KRONOS FUSION ENERGY

PAPER 2.42 · THE KRONOS 2026 SERIES

Plasma-Material Interaction in a Compact Spherical-Tokamak Breeder: Sputtering, Net Erosion, and Redeposition Setting the Plasma-Facing-Surface Lifetime

The lifetime of a plasma-facing surface is set one incident ion at a time: the ion flux erodes the wall by physical sputtering, part of the eroded material returns by...

Read it live — 3-D model · physics validator · film series

BY P I FORD, R J WEGGEL AND C WEGGEL

2026 · EDITORIAL EDITION

THE OFFICIAL RECORD

What this document is, and how to read its numbers

This is a combined editorial. It gathers, in one volume, the two design studies Kronos Fusion Energy released in 2026 — a compact spherical-tokamak tritium/helium-3 breeder and a deuterium–helium-3 tandem-mirror generator — together with the intellectual-property estate, the people, and, in the internal edition, the full commercial case. The scientific text is the same text that appears in the arXiv preprints and the journal submissions; the editorial adds the apparatus a reader needs to hold the whole program at once, and nothing in the physics is altered to fit it.

THE HONESTY STANCE IS THE ASSET

Every headline quantity carries an **evidence class** — DERIVED RECOMPUTED MEASURED REQUIREMENT — and, where a number is a modelled extrapolation rather than a demonstrated value, it is labelled as such and its downside is shown next to it. Several quantities in the underlying corpus moved after first publication; where a value has been withdrawn or restated, the record says so plainly. This is deliberate: a diligence team will find the load-bearing assumptions, so the document surfaces them first.

TWO EDITIONS

This volume is issued in two editions. The **public edition** (light) carries the physics and the design only — no dollar, price, or per-kilogram figure appears anywhere in it. The **internal edition** (dark) adds the economics, the funding architecture, and the defense-commercial analysis, and is marked *Confidential* accordingly; it is not for public distribution. Where the commercial case rests on a modelled assumption rather than a demonstrated one, it is labelled as such and its downside is shown alongside it, on the same terms as the physics.

TITLE	The Kronos Fleet — Hyperion · Aegis · MetroVolt: A Combined Design & Commercialization Study
AUTHOR	Priyanca Ford, Founder & CEO, on behalf of Kronos Fusion Energy
EDITION	2026 Combined Editorial · first issue
COMPANION WORKS	The five-paper arXiv drop — (1) Breeder, (2) Burner, (3) REBCO magnet & tape, (4) Direct Energy Conversion, (5) AI/ML/Quantum control — with matching numbered Zenodo deposits, plus the IOP journal and IAEA-FEC submissions. Patents were filed before the drop.
NAMING	Hyperion = the breeder; Aegis (defense) and MetroVolt (data-center) = one generator in two housings. Internal mode letters (D1, L) do not appear on public surfaces.
STATUS	Conceptual design & simulation study. Nothing herein is a construction commitment.

HOW TO READ THIS VOLUME

The fleet at a glance, and the way its numbers are marked

This volume opens with *Orientation*, presents the five research papers as a bound sequence, and closes with the *Apparatus*. *Foundations* sets out the three general results both machines rest on. *Paper One* is the Hyperion breeder; *Paper Two* the Aegis / MetroVolt generator; *Papers Three, Four and Five* are the enabling science — high-field REBCO magnets and tape, direct energy conversion, and the AI / ML / quantum control stack. A *Digital Twin & 3-D Model* part follows, then the *Environmental* profile. The *Economics* and levelized cost and the *Business Case* and diligence record appear in the internal edition only; the *Simulations* proof record and the Apparatus — patent portfolio, team, limitations, and sources — close both editions.

THE FLEET AT A GLANCE

	HYPERION	AEGIS	METROVOLT
Role	Strategic-isotope foundry	Defense installation power	Campus power
Machine	**Spherical tokamak**	**Tandem mirror**	**Tandem mirror**
Fuel	Deuterium–tritium	Deuterium–helium-3	Deuterium–helium-3
Delivers	Tritium · ^{3}He · 14 MeV n	Resilient installation power	Firm campus power
Physics bar	**Fusion gain only**	Closure (gates named)	Closure + lunar ^{3}He
In the fleet	Breeds the fuel	Proves the generator	Commercial destination

HOW THE NUMBERS ARE MARKED

Every headline quantity carries an evidence class — DERIVED from first principles, RECOMPUTED from raw data, MEASURED in hardware, or a REQUIREMENT yet to be met. Financial figures carry a case label and are confined to the internal (confidential) edition. Values that moved after first publication are shown as withdrawn or restated rather than quietly changed. A capability you can evaluate is one whose limits are on the page.

ABSTRACT

Plasma-Material Interaction in a Compact Spherical-Tokamak Breeder: Sputtering, Net Erosion, and Redeposition Setting the Plasma-Facing-Surface Lifetime

The lifetime of a plasma-facing surface is set one incident ion at a time: the ion flux erodes the wall by physical sputtering, part of the eroded material returns by redeposition, and the difference — net erosion — fixes how long an armour tile lasts and how much high-Z material migrates into the plasma. We pose the erosion source term for the plasma-facing surfaces of the Hyperion breeder (design point $P_{\text{fus}} = 85.04$ MW, $Q = 3.076$, $I_p = 9.66$ MA, negative triangularity $\delta = -0.30$, $B_0 = 8$ T, elongation $\kappa = 2.0$, major radius $R_0 = 1.20$ m, aspect ratio $A = 2.5$) as a formal binary-collision transport problem, and solve it with the high-performance Monte-Carlo binary-collision code RustBCA over a 36-case matrix of deuterium, tritium and helium ions on a tungsten first wall and on the candidate low-activation divertor alloy $Ta_{32}Re_{26}W_{18}Ti_{14}V_{10}$, spanning 100–1000 eV and 0–60° incidence. The headline is a benign, literature-anchored erosion budget. The deuterium-on-tungsten yield peaks at 1.35×10^{-2} atoms\,ion^{-1}, sitting on the accepted value of order 10^{-2}, and is identically zero at 100 eV because that energy lies below the analytic sputtering threshold $E_{\text{th}} \simeq 213$ eV that the same collision theory predicts; across all species the tungsten surface peaks at 8.9×10^{-2} atoms\,ion^{-1} at the helium-1000 eV, 60° corner. The divertor alloy peaks higher, at 1.44×10^{-1} atoms\,ion^{-1}, and we show quantitatively that its erosion is carried by the light titanium and vanadium constituents, which sputter above threshold across the whole energy range while the heavy tungsten, tantalum and rhenium stay below threshold up to 300 eV; in steady state this drives a self-limiting altered surface layer enriched in the heavy, low-yield species. Converting yields to a recession budget shows that at the sub-threshold impact energies of detached-divertor operation the effective yield collapses and net erosion is sub-monolayer per pulse. The reference yield map fixes the physical-sputtering source term on which the surface-erosion budget and the real-time erosion/redeposition tracker are built. The one honest gate is that these are physical-sputtering yields in the binary-collision approximation, without chemical sputtering or redeposition-resolved surface evolution, both of which reduce net erosion below the source-term values reported here.

Open-access deposit (code & data, CC BY 4.0): DOI 10.5281/zenodo.22645885 · Zenodo community *kronos_fusion_energy*. Explore it live: interactive 3-D model · physics validator.

Keywords: plasma-material interaction · physical sputtering · net erosion · redeposition · tungsten · divertor alloy · RustBCA · spherical-tokamak breeder

CONTENTS

Table of Contents

NOMENCLATURE

Symbols, units, and the names of things

Q	plasma (fusion) gain, P_{fus}/P_{aux}
Q_E	engineering gain, net electric out / recirculating in
H_{98}	confinement enhancement over the IPB98(y,2) scaling
Z_{eff}	effective ion charge
c_{ee}	electron–electron bremsstrahlung leading coefficient, 2.120022 (exact)
τ_E	energy confinement time
I_p	plasma current
R_0, a	major radius, minor radius
κ, δ	elongation, triangularity
β_N	normalized plasma beta (Troyon-normalized)
TBR	tritium breeding ratio
DEC	direct energy conversion
CF	plant capacity factor (availability)
FOAK / NOAK / BOAK	first / n^{th} / best of a kind
Hyperion	the ST breeder (internal: Mode D2)
Aegis	the generator, defense/installation housing (internal: Mode M)
MetroVolt	the generator, data-center housing (Mode M)

§ 1

Introduction

WHY THE SURFACE SETS THE LIFETIME

A magnetically confined plasma touches its material boundary through a thin sheath, and every ion that crosses that sheath and strikes the wall can dislodge one or more surface atoms. The cumulative effect — physical sputtering — is the primary erosion channel for the refractory metals that a reactor first wall and divertor are built from [1,2,3]. Net erosion, the sputtered flux minus the fraction that promptly redeposits, determines three coupled outcomes: how long an armour tile survives before it must be replaced, how much high-Z material migrates into the confined plasma as a radiating impurity, and how the surface morphology and composition evolve under ion bombardment [4,5,6]. For a compact, high-power-density breeder the question is quantitative rather than qualitative: at the design-point ion flux and impact energy, is erosion a slow, management-level process, or does it set a hard component-lifetime limit?

The Hyperion breeder is a compact spherical tokamak (ST) operated as a strategic-materials platform — a source of tritium, helium-3 and $14\,\mathrm{MeV}$ neutrons rather than a net-electric plant [7]. An ST confines a large plasma current in a small volume behind a high-field centrepost [8,9], which concentrates the exhaust and makes the plasma-facing surfaces a load-bearing part of the design. The device runs a tungsten first wall and a low-activation refractory divertor at the frozen operating point $P_{\mathrm{fus}} = 85.04\,\mathrm{MW}$, $Q = 3.076$, $I_p = 9.66\,\mathrm{MA}$, $\delta = -0.30$, $B_0 = 8\,\mathrm{T}$, $\kappa = 2.0$, $R_0 = 1.20\,\mathrm{m}$ and $A = 2.5$, with a neutron wall load of $1.885\,\mathrm{MW\,m^{-2}}$ and a first-wall neutron flux of $5.63 \times 10^{18}\,\mathrm{m^{-2}s^{-1}}$. The conventional divertor target would see an unmitigated parallel heat flux of 340–$1570\,\mathrm{MW\,m^{-2}}$, far above the $\sim 10\,\mathrm{MW\,m^{-2}}$ engineering limit, so detachment is mandatory and the target is designed to run cold and partially detached [10,11]. That operating choice, we will show, is exactly what holds sputtering below threshold.

PHYSICAL SPUTTERING AND PRIOR ART

Physical sputtering has a mature quantitative theory. Sigmund's linear-cascade analysis relates the yield to the nuclear energy deposited near the surface and the surface binding energy [12]; Bohdansky reduced this to a compact fit with an explicit energy threshold [13]; and Yamamura and Tawara compiled and parameterised experimental and simulated yields for essentially every ion–target pair of interest, including the angular dependence [14]. Numerically, the binary-collision approximation (BCA) — following each ion through a sequence of screened two-body collisions and counting recoils that escape the surface — has been the workhorse since TRIM and its dynamic descendants [15,16,17], and remains the method of record for tungsten erosion in ITER-class analyses [3,18]. Tungsten is the reference plasma-facing material precisely because its high threshold and low yield make it erode slowly under the light hydrogenic ions of the boundary plasma [19,20], while its erosion under helium and self-sputtering, and the migration and redeposition of the eroded flux, remain the quantities that dedicated erosion codes such as ERO resolve [5,21].

Two features of the present system push beyond the standard tungsten-wall analysis. First, the divertor armour is not elemental tungsten but a five-component low-activation refractory alloy, $Ta_{32}Re_{26}W_{18}Ti_{14}V_{10}$, engineered for near-neutral activation [22,23]; a multicomponent target sputters preferentially, its light constituents leaving faster than its heavy ones, and the surface composition therefore evolves away from the bulk. Second, the operating point is a deliberately cold, detached target, so the relevant impact energies sit near or below the sputtering threshold, where the yield is a steep function of energy and small errors in the boundary model translate into large errors in erosion. Both features demand a species-resolved, energy- and angle-resolved collision calculation rather than a single tabulated yield.

CONTRIBUTION

This paper answers the first, load-bearing half of the lifetime question — the physical-sputtering source term — with direct BCA modelling, and states it as a formal transport problem so that the numbers are reproducible and the approximations explicit. Specifically we

derive the governing binary-collision transport, the analytic sputtering-yield and threshold laws it reduces to, and the net-erosion surface balance including the preferential-sputtering altered-layer steady state (section 2);
compute the full 36-case yield map on tungsten and on the divertor alloy with the GPU-HPC-campaign code RustBCA, and quantify its numerical convergence (sections 3–4);
show that the deuterium-on-tungsten peak of 1.35×10^{-2} atoms\,ion^{-1} reproduces the accepted literature value and that the code's own 100 eV zeros coincide with the analytic threshold, an internal validation (section 4);
convert the yields to a recession budget, demonstrate the sub-monolayer-per-pulse margin at design-point detached-target energies, and identify the light-element-carried erosion of the alloy as the design-relevant material-selection quantity (section 5); and
hand the validated yield map to the surface-lifetime budget and to the real-time erosion/redeposition tracker built on it, stating honestly what the source-term calculation does and does not yet include (sections 6–7). enumerate

Every yield traces to the frozen anchor serial BR-L2-A27 in the Kronos physics de-risking campaign [27], independently re-run and reproduced.

§ 2

Governing equations and the formal problem

BINARY-COLLISION TRANSPORT

The BCA treats the passage of an energetic ion through a solid as a sequence of independent elastic two-body collisions with target atoms, interspersed with continuous electronic energy loss. Between collisions the projectile travels a mean free path $\lambda = n^{-1/3}$ set by the target atomic number density n. Each collision is governed by a screened-Coulomb interatomic potential

$$V(r) = \frac{Z_1 Z_2 e^2}{4\pi\varepsilon_0\, r}\,\Phi\left(\frac{r}{a}\right),$$

where Z_1, Z_2 are the projectile and target atomic numbers, Φ is a universal screening function (we use the Kr–C / ZBL form [24,16]), and the screening length is the Lindhard/universal length

$$a = \frac{0.8854\, a_0}{(Z_1^p + Z_2^p)^{1/2}}, \qquad a_0 = 0.529\,\backslash\text{AA},$$

with $p = 2/3$ (Lindhard) or the ZBL exponent 0.23. For a projectile of laboratory energy E, impact parameter b and reduced (centre-of-mass) energy $E_c = E\, M_2/(M_1 + M_2)$, the classical centre-of-mass scattering angle θ follows from the scattering integral

$$\theta(E,b) = \pi - 2b\int_{r_{\min}}^{\infty} \frac{\mathrm{d}r}{r^2\sqrt{1 - \dfrac{V(r)}{E_c} - \dfrac{b^2}{r^2}}},$$

where the distance of closest approach $r_{\min}$ is the largest root of the radicand. The elastic energy transferred to the recoiling target atom is

$$T = \gamma\, E\, \sin^2\left(\frac{\theta}{2}\right), \qquad \gamma \equiv \frac{4M_1M_2}{(M_1+M_2)^2},$$

with γ the maximum fractional energy transfer. Electronic (inelastic) losses along the path are treated in the Lindhard–Scharff low-velocity regime,

$$\left(\frac{\mathrm{d}E}{\mathrm{d}x}\right)_e = k_L\sqrt{E},$$

with k_L the Lindhard electronic-stopping coefficient, partitioned between a local (impact-parameter-dependent) and a nonlocal contribution [15,37].

RECOIL CASCADE AND THE SURFACE-ESCAPE CONDITION

Recoils created with T above a bulk displacement cutoff propagate the collision cascade recursively, generating further recoils, until every fragment falls below a tracking cutoff E_{cut} of order the surface binding energy. A recoil that reaches the surface is emitted — and counted as sputtered — only if the component of its kinetic energy normal to the surface exceeds the planar surface binding barrier E_s,

$$E\cos^2\alpha \;>\; E_s,$$

α being the emission angle from the surface normal; an isotropic (spherical) barrier replaces the left side by E. The sputtering yield is the ensemble average

$$Y(E,\theta_{\text{inc}}) \;=\; \frac{\langle N_{\text{sput}}\rangle}{N_{\text{inc}}},$$

the mean number of emitted target atoms per incident ion at energy E and incidence angle θ_{inc} from the surface normal. Equations 1–7 are the complete forward model; RustBCA evaluates them by Monte-Carlo sampling, and everything below is either an analytic reduction of this model used for verification, or a post-processing of its output into an erosion budget.

ANALYTIC YIELD, THRESHOLD AND ANGULAR LAWS

For verification we use the reduced forms the cascade theory collapses to. Introduce the dimensionless Lindhard reduced energy

$$\varepsilon = \frac{M_2}{M_1 + M_2} \, \frac{a}{Z_1 Z_2 e^2/4\pi\varepsilon_0} \, E,$$

and the Kr–C reduced nuclear stopping cross-section in the Wilson–Haggmark–Biersack approximation

$$s_n(\varepsilon) = \frac{0.5 \, \ln(1 + 1.2288\,\varepsilon)}{\varepsilon + 0.1728\sqrt{\varepsilon} + 0.008\,\varepsilon^{0.1504}}.$$

The Bohdansky–Yamamura yield at normal incidence is

$$Y(E) = Q\, s_n(\varepsilon)\, \left[1 - \left(\frac{E_{\rm th}}{E}\right)^{2/3}\right] \left(1 - \frac{E_{\rm th}}{E}\right)^2,$$

with Q a material yield factor and $E_{\rm th}$ the sputtering threshold energy, below which $Y \equiv 0$. The threshold is set by the surface binding energy and the kinematics: for a light projectile ($M_1/M_2 \lesssim 0.3$)

$$E_{\rm th} = \frac{E_{\rm s}}{\gamma\,(1-\gamma)},$$

while for heavier projectiles $E_{\rm th} \simeq 8\, E_{\rm s}\, (M_1/M_2)^{2/5}$. The angular dependence follows the Yamamura form

$$\frac{Y(E,\theta_{\rm inc})}{Y(E,0)} = \big(\cos\theta_{\rm inc}\big)^{-f} \, \exp\Big\{ f\big[1 - (\cos\theta_{\rm inc})^{-1}\big] \cos\theta_{\rm opt} \Big\},$$

which rises with $\theta_{\rm inc}$ from normal incidence toward a maximum near a species-dependent optimum $\theta_{\rm opt}$ before falling as reflection takes over. Equation 11 is quantitatively predictive here: for deuterium ($M_1 = 2.014$) on tungsten ($M_2 = 183.84$), $\gamma = 0.0426$ and, with the tungsten surface binding energy $E_{\rm s} = 8.68$ eV, $E_{\rm th} = 213$ eV. That single number anticipates the code result — a zero yield at 100 eV and a finite yield at 300 eV — and is the internal check we exploit in section 4. Table 1 lists the thresholds for the ions and the key target elements.

TARGET ($E_{\rm s}$/EV)	$\gamma_{\rm D}$	$E_{\rm th}$(D)/EV	$E_{\rm th}$(T)/EV	$E_{\rm th}$(HE)/EV
W (8.68)	0.043	213	147	114
Ta (8.10)	0.043	198	137	107
Re (8.03)	0.043	196	136	106
Ti (4.85)	0.130	43	31	25
V (5.31)	0.114	53	38	30

Analytic sputtering thresholds $E_{\rm th}$ from equation 11 using surface binding energies $E_{\rm s}$, for the three incident ions on tungsten and on the light and heavy constituents of the divertor alloy. Light constituents (Ti, V) have both lower $E_{\rm s}$ and lighter mass, hence far lower thresholds; this ordering is what makes the alloy's erosion light-element-carried.

FROM YIELD TO NET EROSION

The sputter yield is the source term of a surface mass balance. An ion flux $\Gamma_{\rm ion}$ (m^{-2}s^{-1}) of impact energy E and angle $\theta_{\rm inc}$ produces a gross erosion flux

$$\Gamma_{\rm ero} = \Gamma_{\rm ion}\, Y(E, \theta_{\rm inc}),$$

of which a fraction R promptly redeposits within an ionization/gyration length of the surface. The surface recedes at

$$\dot z = \frac{\Gamma_{\rm ero} - \Gamma_{\rm redep}}{n} = \frac{\Gamma_{\rm ion}\, Y}{n}\,(1-R),$$

with n the target atomic number density (tungsten $n_{\mathrm{W}} = 6.31 \times 10^{28}\,\mathrm{m}^{-3}$; the alloy $n_{\mathrm{alloy}} = 6.13 \times 10^{28}\,\mathrm{m}^{-3}$). Prompt redeposition is large for a high-Z species emitted into a strong magnetic field, because the sputtered atom is ionized within a mean free path and returns along its gyro-orbit before it can migrate; $R > 0.9$ is typical for tungsten in reactor conditions [29,21]. A convenient lifetime measure is the per-pulse ion fluence $\Phi = \Gamma_{\mathrm{ion}}\,\tau_{\mathrm{p}}$ that erodes exactly one monolayer of areal density $n_{\mathrm{ML}} = n^{2/3}$ (tungsten $n_{\mathrm{ML}} = 1.58 \times 10^{19}\,\mathrm{m}^{-2}$):

$$\Phi_{\mathrm{ML}} = \frac{n_{\mathrm{ML}}}{Y\,(1 - R)}.$$

Erosion is "sub-monolayer per pulse" whenever $\Phi < \Phi_{\mathrm{ML}}$.

PREFERENTIAL SPUTTERING AND THE ALTERED LAYER

For the multicomponent alloy each constituent i (bulk atomic fraction c_i^{b}) has its own partial yield $Y_i(E,\theta)$, and the total yield entering 13 is $Y = \sum_i c_i^{\mathrm{s}} Y_i$ weighted by the *surface* fractions c_i^{s}. Because the light constituents sputter faster, the surface depletes in them and enriches in the heavy, low-yield constituents until, in steady state, the emitted flux composition matches the bulk (mass conservation through the recession front). Setting the partial emitted flux $c_i^{\mathrm{s}} Y_i$ proportional to the bulk supply $c_i^{\mathrm{b}} \bar{Y}$ gives the altered-layer steady state

$$\frac{c_i^{\mathrm{s}}}{c_i^{\mathrm{b}}} = \frac{\bar{Y}}{Y_i}, \qquad \bar{Y} \equiv \left(\sum_j c_j^{\mathrm{b}}/Y_j\right)^{-1},$$

so the surface enriches in exactly the components with the smallest partial yield (W, Ta, Re) and depletes in the light Ti, V. Equation 16 is self-limiting: as the surface enriches in the low-yield species the total yield falls toward the heavy-element value, which is why the transient light-element loss does not run away. The time-resolved version of 16, coupled to 14, is exactly the surface-evolution problem the erosion/redeposition tracker integrates; here we compute its inputs — the partial yields $Y_i(E,\theta)$ — from first collisions.

CLOSING THE BOUNDARY: IMPACT ENERGY FROM THE SHEATH

The impact energy that enters 10 is not free: it is fixed by the sheath that forms at the surface. An ion of charge Z falling through the combined Debye and pre-sheath potential arrives with

$$E_{\mathrm{imp}} \simeq 2\,T_i + 3\,Z\,T_e,$$

T_i, T_e being the local ion and electron temperatures at the sheath entrance [30,31]. This closes the model: the divertor is designed to run detached with a cold target, T_e of a few eV, so by 17 the hydrogenic impact energies are tens of eV — below the tungsten thresholds of table 1. Equations 1–17 constitute the formal problem; the remainder of the paper solves and evaluates it.

§ 3

Computational methodology: the GPU-HPC campaign

SOLVER

The forward model 1–7 is solved with RustBCA, a modern, high-performance implementation of the binary-collision approximation [25,26]. RustBCA follows each incident pseudo-ion and its recursive recoil cascade through the amorphous-target BCA: the free-flight path is drawn from the atomic density; the scattering integral 3 is evaluated for the sampled impact parameter (via the Gauss–Mehler quadrature / MAGIC-formula reduction), returning the deflection and the energy transfer 4; electronic losses 5 are applied along the path; and every recoil is tested against the surface-escape condition 6. Impact parameters are sampled uniformly in b^2 up to $p_{\max} = (\pi n^{2/3})^{-1/2}$, and recoils are tracked recursively down to a cutoff $E_{\text{cut}} = E_{\text{s}}$. The target models are elemental tungsten and the five-component alloy $Ta_{32}Re_{26}W_{18}Ti_{14}V_{10}$, the latter entered as a homogeneous multicomponent solid with per-element masses, atomic numbers and surface binding energies so that partial yields Y_i are resolved natively.

PROBLEM SCALE AND CASE MATRIX

The computation is a 36-case matrix: three incident species (D, T, He) $\times$ three energies (100, 300, 1000 eV) $\times$ two incidence angles ($0°$ and $60°$) $\times$ two targets (W, alloy). Each case launches $N_{\text{inc}} = 1 \times 10^5$ to 5×10^5 incident ions and their full recoil cascades; the alloy cases use the largest samples (5×10^5) because the light-element partial yields must be resolved to several significant figures. The matrix is embarrassingly parallel — cases are independent, and within a case the pseudo-ions are independent — so it maps cleanly onto the heterogeneous accelerator fleet of the Kronos NVIDIA GPU HPC campaign (A100, H100 and A10 nodes), with the per-case BCA ensembles dispatched across the fleet and the summary tallies harvested centrally. The same campaign carries the neutron-transport (OpenMC), first-principles (DFT/MLIP) and edge-transport codes that supply the boundary conditions and the alloy composition, so the PMI source term is computed inside a single, version-controlled evidence pipeline rather than in isolation. No cost or resource-accounting figures are attached to any run; the campaign is described here only to the extent needed for reproducibility.

NUMERICAL CONVERGENCE AND VERIFICATION

The Monte-Carlo estimator 7 has a statistical standard error that scales as $\sigma_Y/Y \sim N_{\text{sput}}^{-1/2}$, so the precision is set by the number of *sputtered* atoms recorded, not by N_{inc} alone. At the alloy peak ($N_{\text{sput}} = 7.2 \times 10^4$ from $N_{\text{inc}} = 5 \times 10^5$) the relative error is 0.4%; at the deuterium-on-tungsten peak ($N_{\text{sput}} = 1.35 \times 10^3$ from 10^5) it is 2.7%; and in the near-threshold tungsten cases (as few as 47 sputtered atoms) it rises to $\sim 15\%$, which is why we report those small yields to two significant figures only. Table 2 collects the convergence statistics for the carrying cases. Three independent verification layers back the matrix: (i) the internal, parameter-free coincidence between the code's 100 eV zeros and the analytic threshold 11; (ii) agreement of the deuterium-on-tungsten peak with the accepted literature yield of order 10^{-2} [14,16]; and (iii) cross-checking against the frozen anchors of the de-risking register and an independent GPU-fleet re-run, under which the serial BR-L2-A27 is stamped “independently re-tested and reproduced” [27,28]. The run used a fixed pseudo-random seed (20260726) so the matrix is regenerable byte-for-byte.

CASE	N_{inc}	N_{sput}	Y (ATOMS ION^{-1})	σ_Y/Y
D → W, 300 eV, 0°	2×10^5	47	2.4×10^{-4}	15%
D → W, 1000 eV, 60°	1×10^5	1352	1.35×10^{-2}	2.7%
He → W, 1000 eV, 60°	1×10^5	8921	8.92×10^{-2}	1.1%
He → alloy, 1000 eV, 60°	5×10^5	71795	1.44×10^{-1}	0.4%

Monte-Carlo convergence for representative cases: incident sample N_{inc}, sputtered count N_{sput}, yield Y and relative statistical error $\sigma_Y/Y \approx N_{\text{sput}}^{-1/2}$. Yields in near-threshold cases carry $\sim 15\%$ error and are reported to two figures.

§ 4

Results: the sputter-yield map

Table 3 and figure 1 collect the headline yields; figures 2–5 resolve them in energy, angle and species. Four results carry the section.

SURFACE / CHANNEL	PEAK YIELD	CORNER	NOTE
deuterium → tungsten	1.35×10^{-2}	1000 eV, 60°	matches literature $\sim 10^{-2}$
any ion → tungsten	8.92×10^{-2}	He, 1000 eV, 60°	mass/energy ordering
divertor alloy (all species)	1.44×10^{-1}	He, 1000 eV, 60°	light Ti/V constituents dominate

Peak physical-sputtering yields from the **36**-case RustBCA matrix (serial BR-L2-A27). Yields are atoms per incident ion; the "corner" names the energy/angle case where the peak occurs.

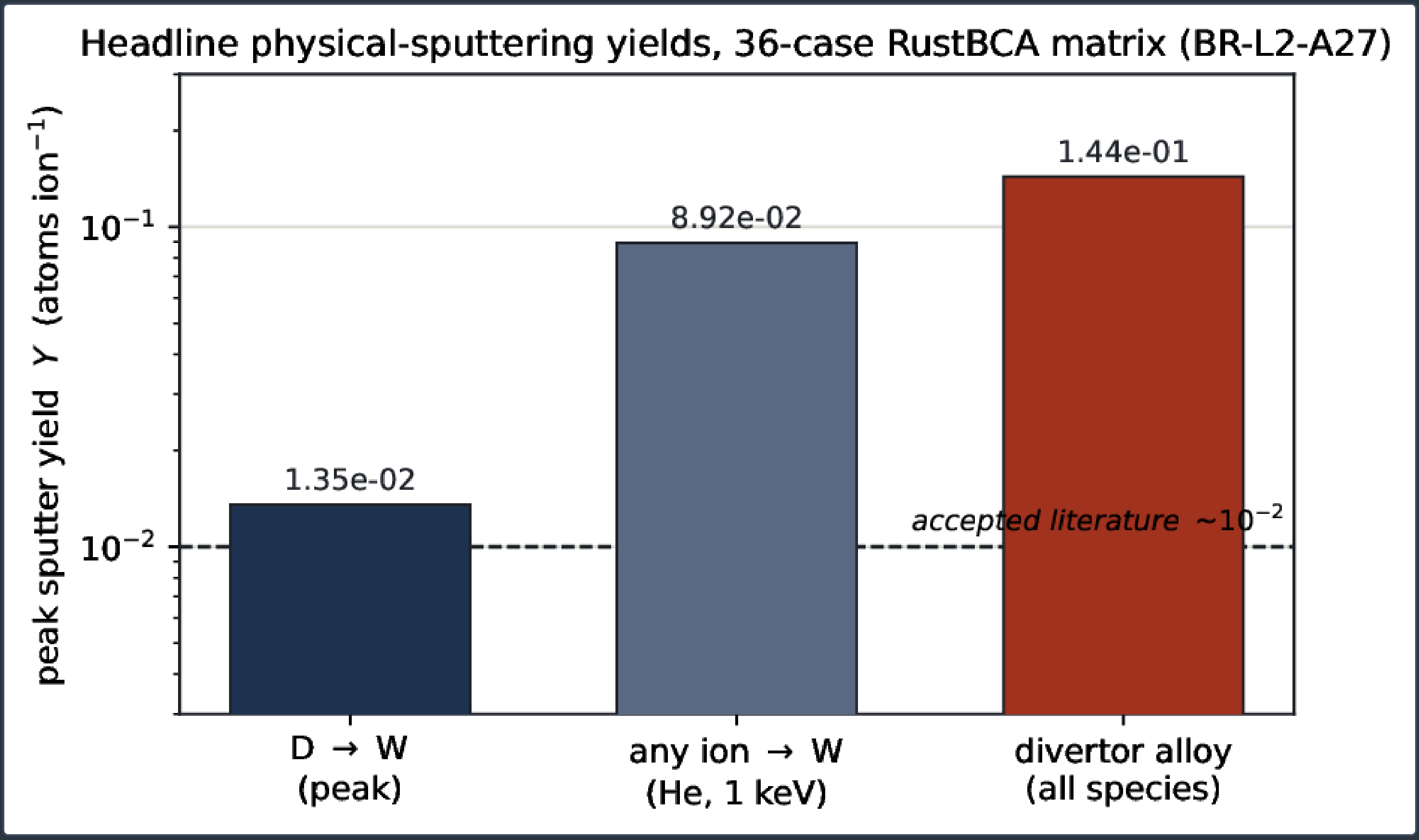

The three carrying peak yields of the matrix. The deuterium-on-tungsten peak sits on the accepted literature value ($\sim 10^{-2}$, dashed); the all-species tungsten peak and the divertor-alloy peak are higher, the latter carried by its light titanium and vanadium constituents. Data from the RustBCA matrix (BR-L2-A27).

The tungsten wall erodes slowly, and does so below threshold. The deuterium-on-tungsten peak yield is 1.35×10^{-2} atoms\,ion^{-1}, reproducing the accepted literature value of order 10^{-2}. Crucially, the code returns an *identically zero* yield at 100 eV for both hydrogenic ions on tungsten (figure 2), because 100 eV lies below the thresholds $E_{th}(D) = 213$ eV and $E_{th}(T) = 147$ eV predicted independently by 11; the first finite yields appear at 300 eV (2.4×10^{-4} for D, 2.6×10^{-3} for T at normal incidence) and climb steeply toward 1000 eV. This parameter-free coincidence between the Monte-Carlo result and the analytic threshold is the strongest internal validation the matrix offers, and it is the physical reason a tungsten wall is chosen: over most of the boundary-plasma energy range it simply does not sputter.

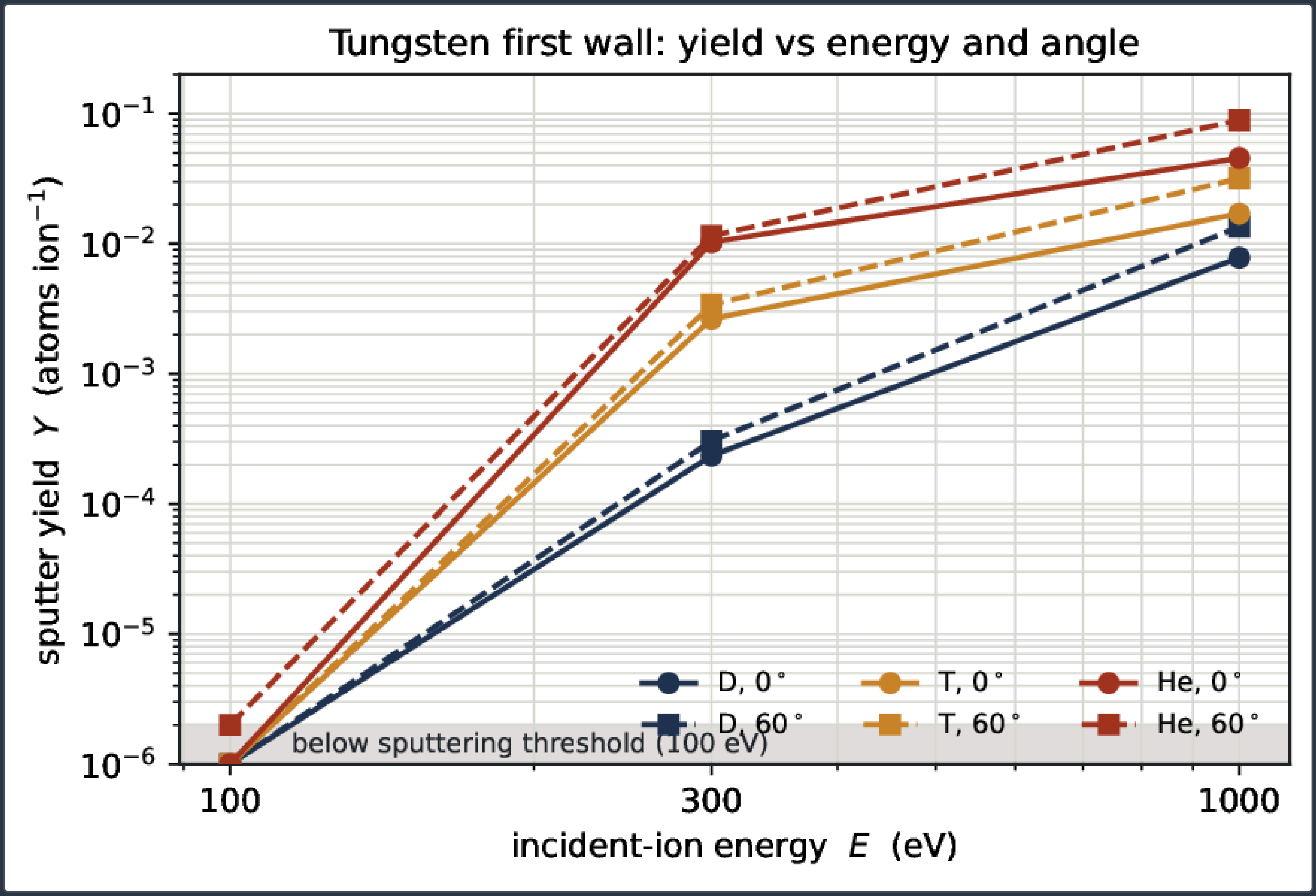

Tungsten first wall: sputter yield versus incident energy for D, T and He at $0°$ (solid) and $60°$ (dashed). The hydrogenic yields vanish at 100 eV — below the analytic threshold — and rise steeply above it; helium, with the lowest threshold and largest mass, leads at every energy. Points below the shaded floor are exact zeros from the code.

Helium leads, by mass and threshold. The all-species tungsten peak of 8.92×10^{-2} atoms\,ion^{-1} occurs at the helium-1000 eV, $60°$ corner. Helium is the heaviest incident ion in the set, so by 4 it deposits the most recoil energy near the surface, and it has the lowest hydrogen-like threshold ($E_{th} \simeq 114$ eV), so it is the only ion with a measurable yield already at 100 eV (2×10^{-6} at $60°$, right at threshold). The full energy/angle ordering — helium above tritium above deuterium, oblique above normal — is exactly the mass- and energy-dependence of the nuclear-stopping cross-section 9, and it holds without exception across the matrix.

The alloy's erosion is carried by its light constituents. The alloy peak yield, 1.44×10^{-1} atoms\,ion^{-1}, is higher than tungsten's, and figure 3 shows why: titanium and vanadium carry the yield. At 100 eV the alloy still sputters (6.6×10^{-4} atoms\,ion^{-1} for deuterium) entirely through Ti and V, whose thresholds (43 and 53 eV for deuterium, table 1) lie well below 100 eV, while the heavy W, Ta and Re contribute nothing until 300 eV and only become comparable at 1000 eV. At the alloy peak the partial yields are $Y_{Ta} = 3.7 \times 10^{-2}$, $Y_{Ti} = 3.3 \times 10^{-2}$, $Y_{Re} = 3.0 \times 10^{-2}$, $Y_V = 2.3 \times 10^{-2}$ and $Y_W = 2.1 \times 10^{-2}$: only at 1 keV does the heavy fraction catch up. The practical reading, through the altered-layer steady state 16, is that the surface enriches in the heavy species and depletes in Ti and V, self-limiting the total yield — and that preferential sputtering of the light constituents is the design-relevant quantity a divertor material selection must weigh, exactly the species-resolved detail a binary-collision model exists to provide.

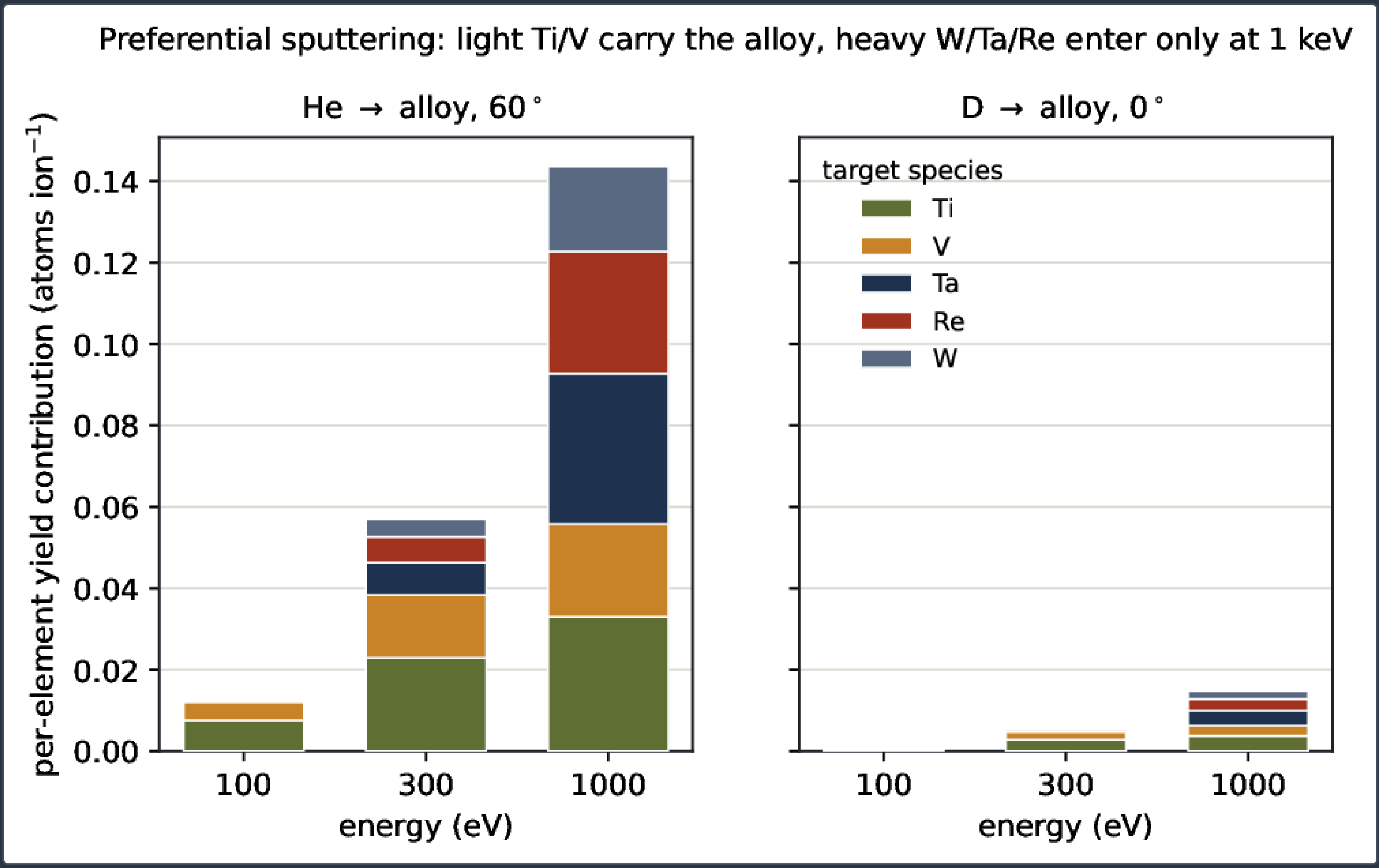

Preferential sputtering of the divertor alloy. Stacked per-element contributions to the total yield versus energy, for helium at 60° (left) and deuterium at 0° (right). Light Ti and V carry the yield at 100–300 eV; the heavy W, Ta and Re sit below threshold up to 300 eV and only enter at 1 keV. Data from the RustBCA matrix (BR-L2-A27).

The alloy erodes above tungsten, case for case. Plotting the alloy total yield against the tungsten yield for every matching case (figure 4) puts every point above the diagonal: the alloy erodes faster than elemental tungsten under identical bombardment, by roughly an order of magnitude near threshold (where only the alloy's light species are active) narrowing to a factor of 1.6 at the 1 keV corner (where tungsten's own yield has risen). This is the quantitative penalty of the low-activation composition, and it is bounded and known. Figure 5 shows the angular enhancement 12 directly: oblique (60°) incidence raises the yield over normal incidence by factors of 1.1–2.0 across the matrix, consistent with the grazing-angle rise of the linear-cascade theory below its reflection-dominated optimum.

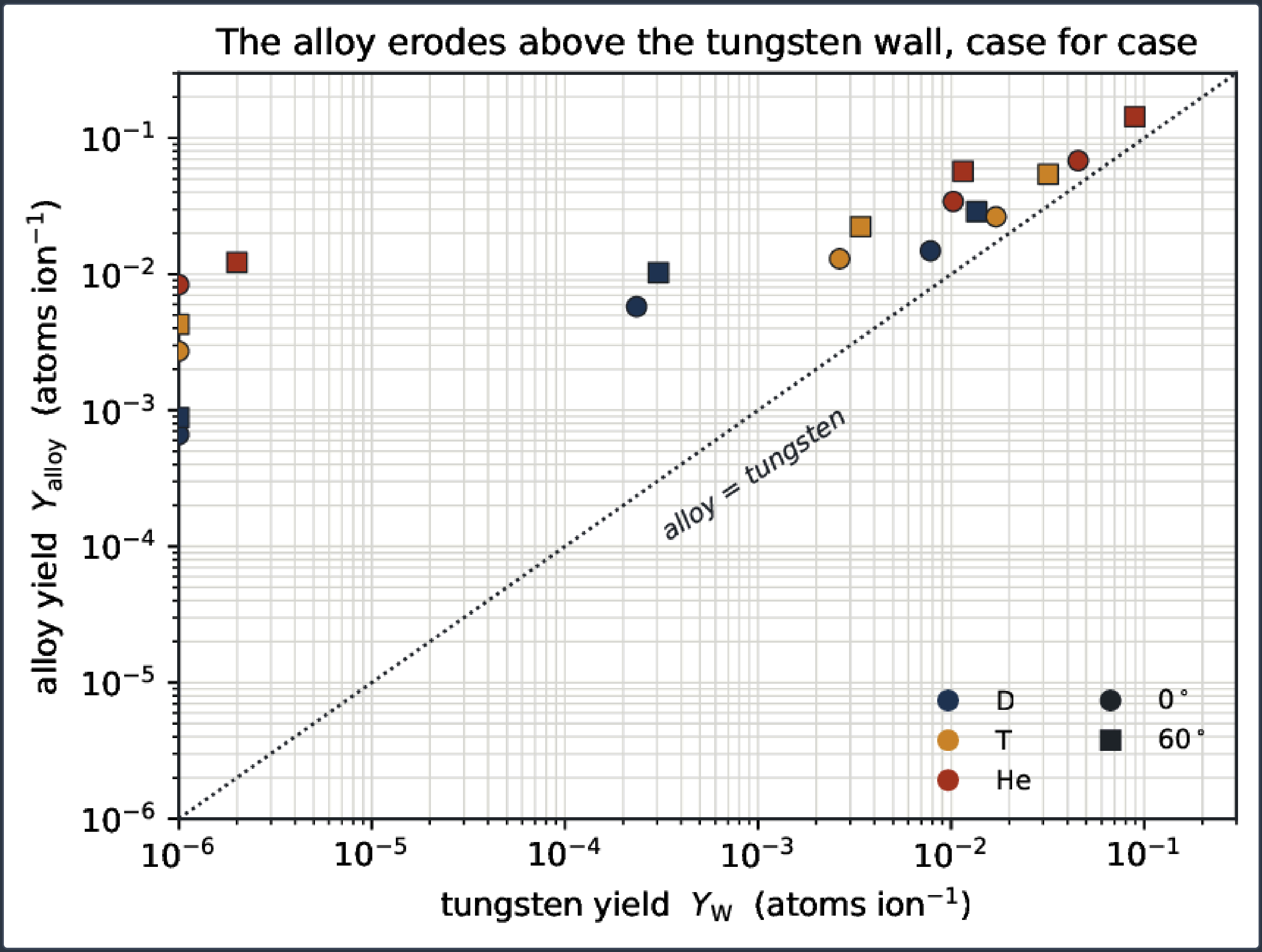

Case-by-case comparison of the alloy total yield against the tungsten yield (matched species, energy and angle). Every point lies above the diagonal: the low-activation alloy erodes faster than elemental tungsten, by up to an order of magnitude near threshold.

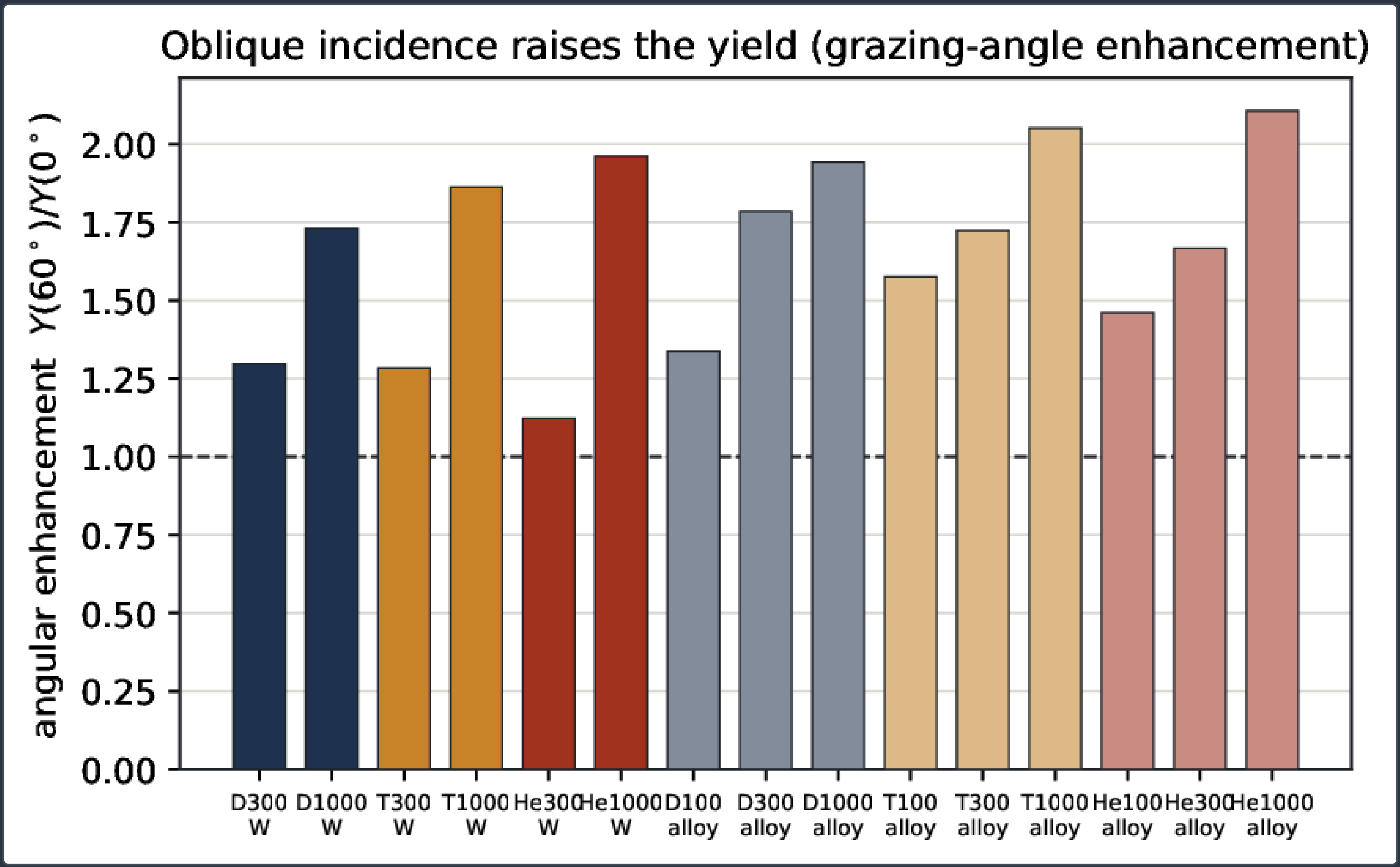

Angular enhancement $Y(60°)/Y(0°)$ for every case with finite yields at both angles. Oblique incidence raises the yield by 1.1–$2.0\times$, the grazing-angle behaviour of equation 12. Darker bars are tungsten, lighter bars the alloy.

§ 5

From yields to a surface-lifetime budget

The yields are the source term for the net-erosion balance 14. Two figures translate the map into a lifetime statement. Figure 6 evaluates the gross recession rate $\dot{z} = \Gamma_{\rm ion} Y/n$ (before any redeposition credit, $R = 0$) at a representative first-wall ion flux $\Gamma_{\rm ion} = 10^{20}\,{\rm m}^{-2}{\rm s}^{-1}$, as a function of impact energy for the three ions on tungsten. The rate is a steep function of energy that follows the yield: it is zero below threshold, reaches a few μm per full-power year at 300 eV, and only at the 1 keV corner climbs to the hundreds of $\mu{\rm m\,fpy}^{-1}$ range. Because the divertor is designed to run detached with a target T_e of a few eV, the design-point impact energies from 17 are tens of eV — the shaded band — where the tungsten yield is below threshold and the recession rate is essentially zero. The wall survives not because the yield is small at every energy but because operation is deliberately kept below the threshold energy.

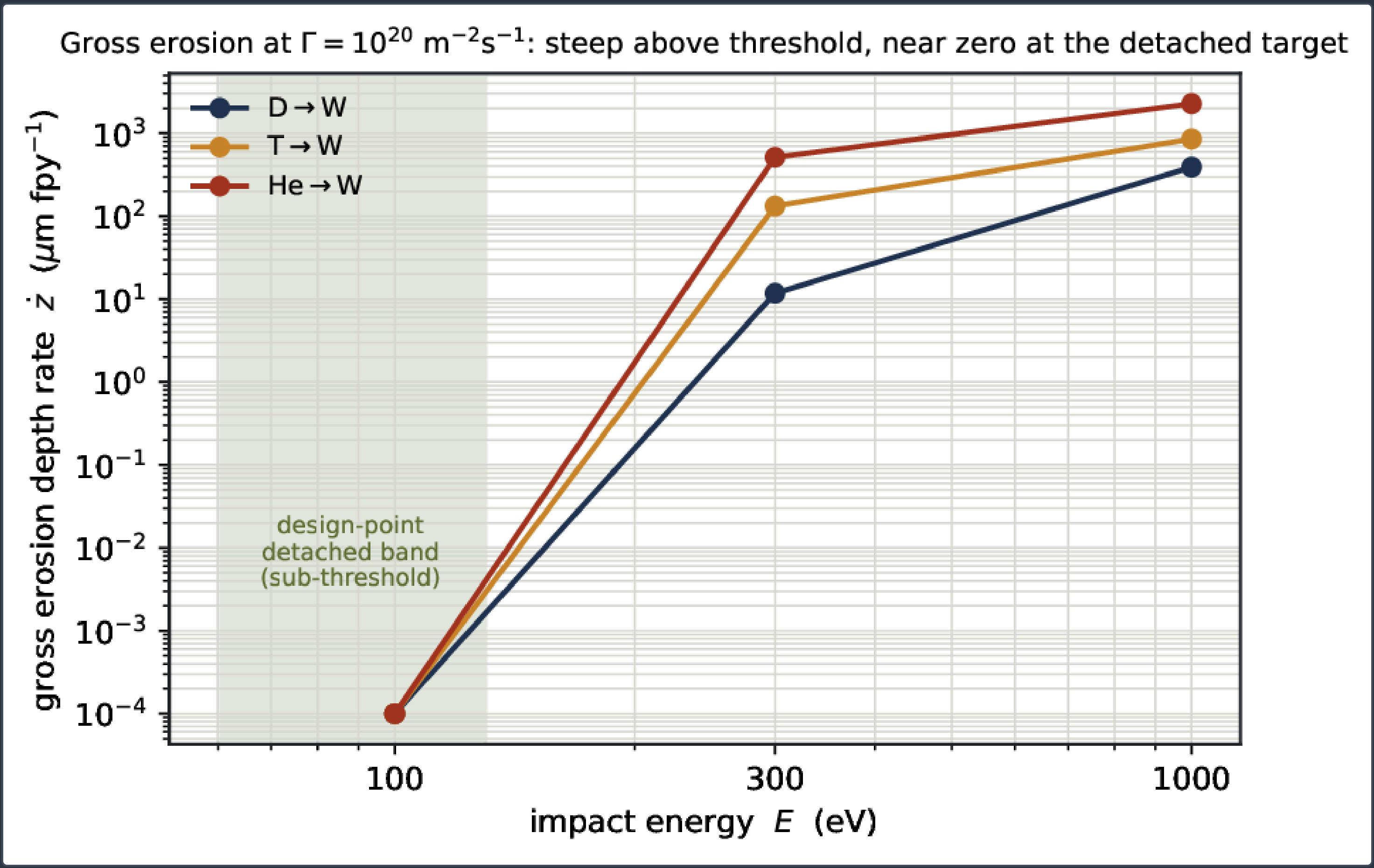

Gross erosion depth rate $\dot{z} = \Gamma_{\rm ion} Y/n$ on tungsten at a representative first-wall ion flux $\Gamma_{\rm ion} = 10^{20}\,{\rm m}^{-2}{\rm s}^{-1}$ (redeposition set to zero, an upper bound), versus impact energy. The rate is zero below threshold and rises steeply above it; the shaded band marks the detached-target energies where the design operates. Derived from the RustBCA yields.

Figure 7 makes the closure explicit. It plots the sheath impact energy 17 against target electron temperature for each ion and overlays the tungsten deuterium threshold band inferred from the matrix (zero at 100 eV, finite at 300 eV, i.e. $E_{\rm th} \approx 160$–230 eV, bracketing the analytic 213 eV). The detached-target T_e band of 1–8 eV maps to hydrogenic impact energies well below the threshold: physical sputtering of the tungsten wall is, by design, an off-nominal-only process. Quantitatively, the sub-monolayer margin follows from 15: at the matrix-peak deuterium yield of 1.35×10^{-2} a per-pulse fluence up to $\Phi_{\rm ML} = n_{\rm ML}/Y = 1.2 \times 10^{21}\,{\rm m}^{-2}$ erodes less than one monolayer even before any redeposition credit, and at the sub-threshold operating energies the tolerable fluence is unbounded because $Y \to 0$ (figure 8). Applying a conservative reactor-typical prompt-redeposition fraction $R \gtrsim 0.9$ divides the net rate by a further order of magnitude. The tungsten first wall therefore sits firmly in the slow-erosion regime, and surface lifetime is a management problem rather than a limit.

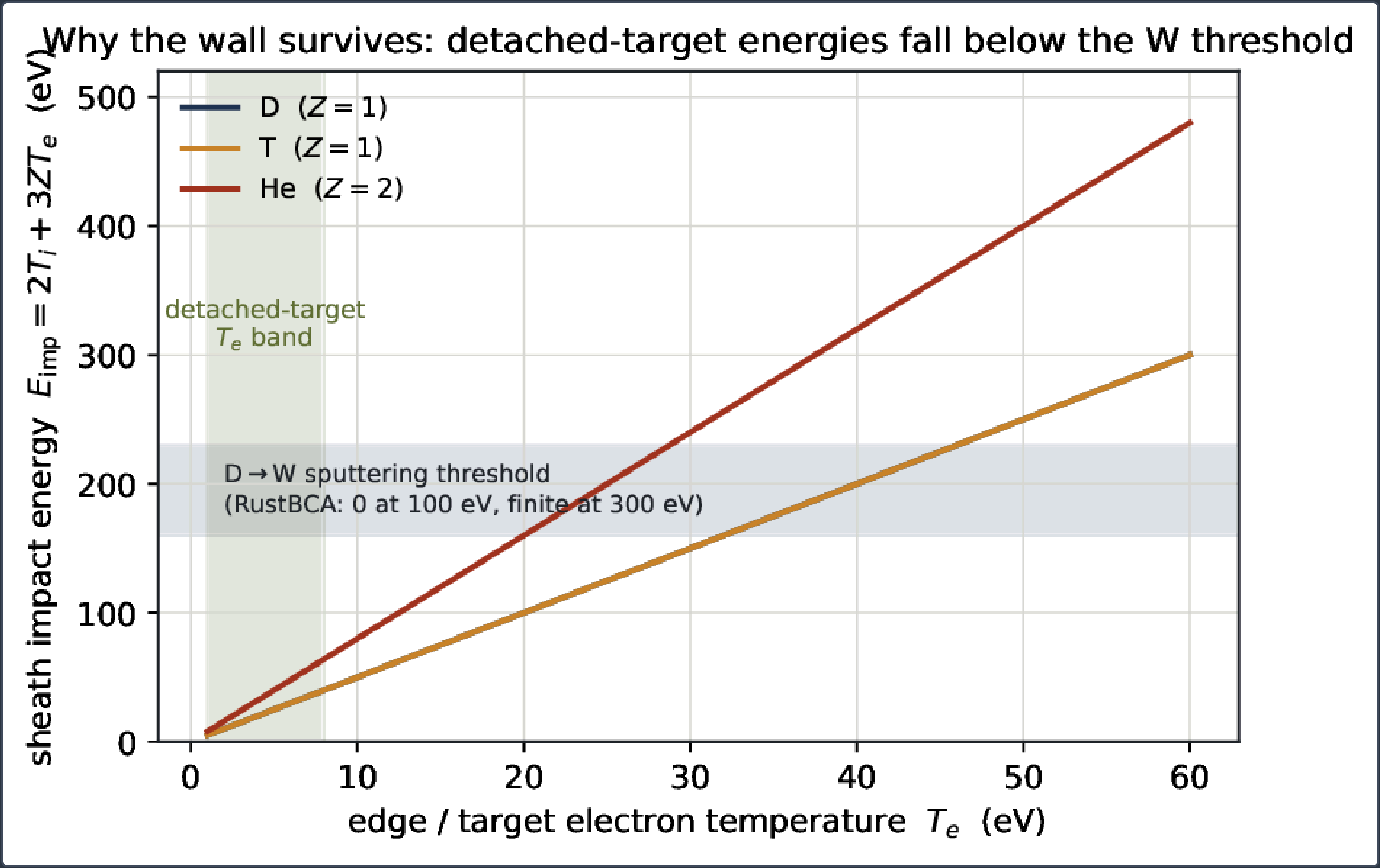

Closure of the boundary model. Sheath impact energy $E_{\text{imp}} = 2T_i + 3ZT_e$ versus target T_e for D, T and He, with the tungsten deuterium sputtering-threshold band (from the RustBCA matrix) shaded. The detached-target T_e band maps to impact energies below threshold, so the wall does not sputter at the design point.

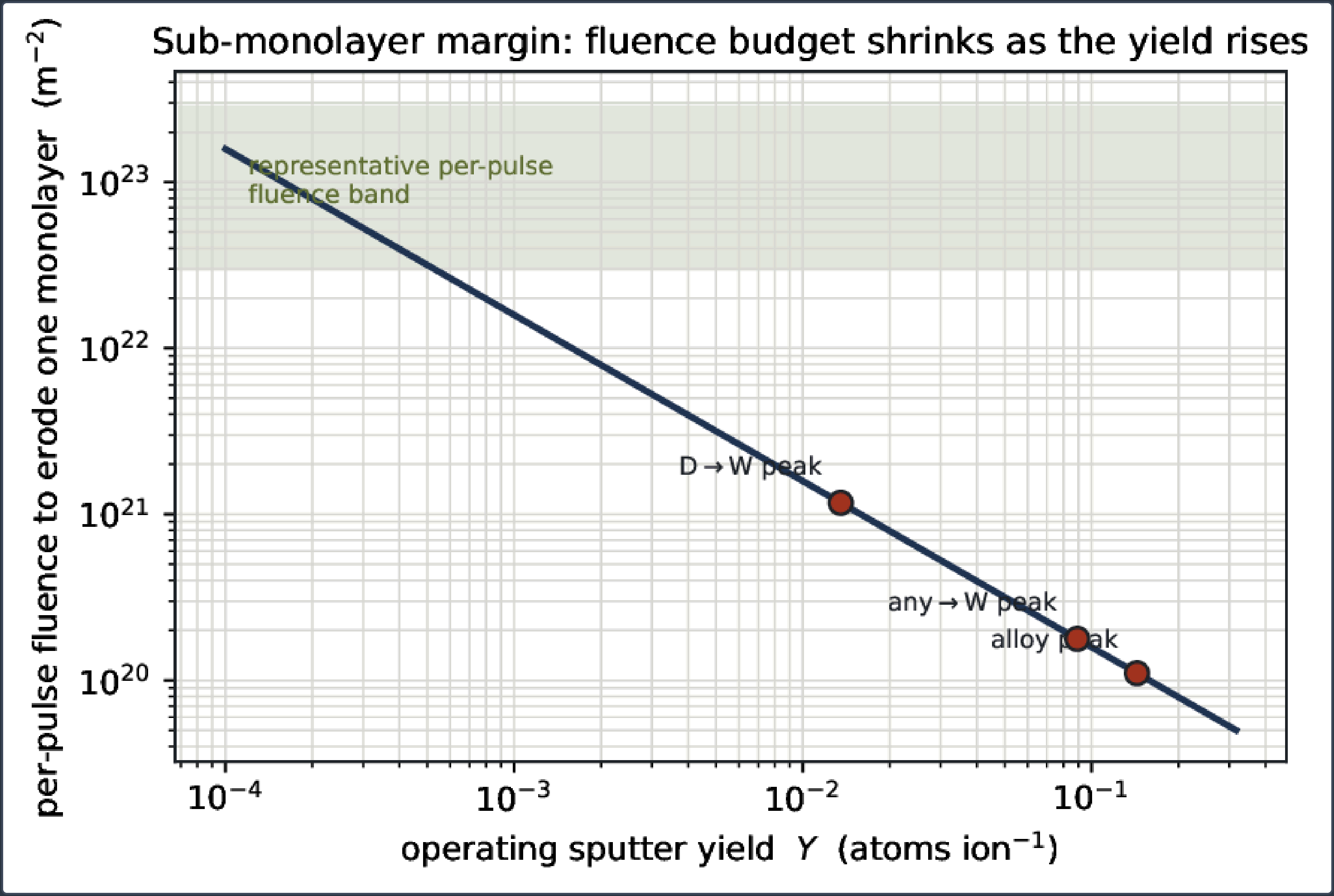

The sub-monolayer statement made quantitative: per-pulse ion fluence that erodes one tungsten monolayer, $\Phi_{ML} = n_{ML}/Y$, versus operating yield. The three matrix peaks are marked; a representative per-pulse fluence band lies below all of them, and at sub-threshold operating energies $\Phi_{ML} \to \infty$.

The alloy divertor carries a tighter but still-tractable budget. Its higher, light-element-weighted yield sets a faster gross recession, but the altered-layer steady state 16 caps the effective yield as the surface enriches in the heavy species, and the strike-point-sweeping and detachment-control strategy is designed precisely to keep the target energy and flux in the low-yield regime [32]. These yields are also the reference against which the real-time erosion/redeposition tracker (feature KFE-CF-BR-033) is validated: the tracker reproduces this RustBCA case set as its ranking check and then extends it to the swept, time-dependent surface map used in operation, closing the loop of figure 9.

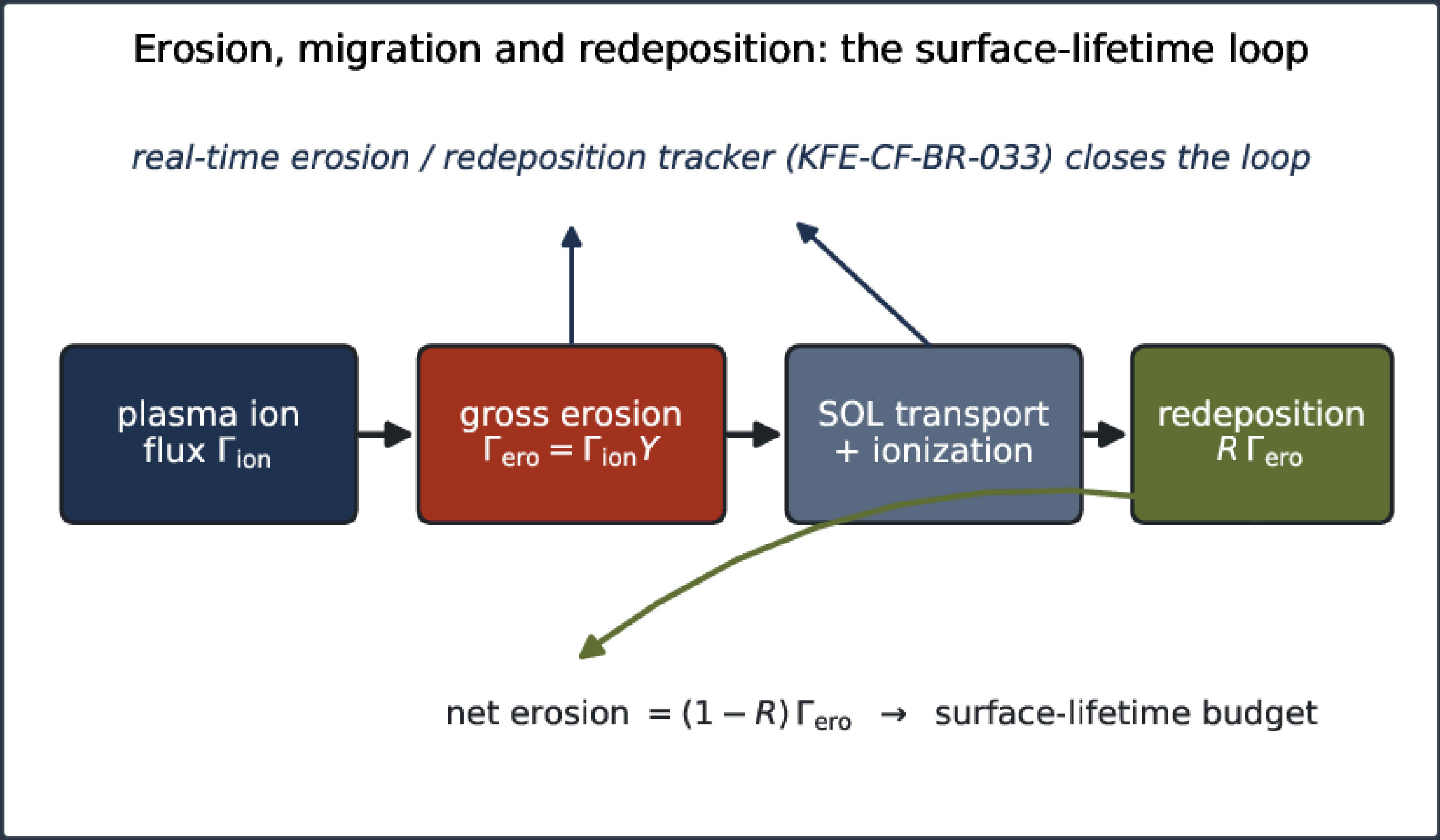

(Schematic.) The surface-lifetime loop. The plasma ion flux drives gross erosion $\Gamma_{ero} = \Gamma_{ion} Y$ (this paper's source term); eroded atoms are transported and ionized in the scrape-off layer and a fraction R promptly redeposits, leaving net erosion $(1 - R)\Gamma_{ero}$. The real-time erosion/redeposition tracker (KFE-CF-BR-033) closes the loop and drives strike-point control.

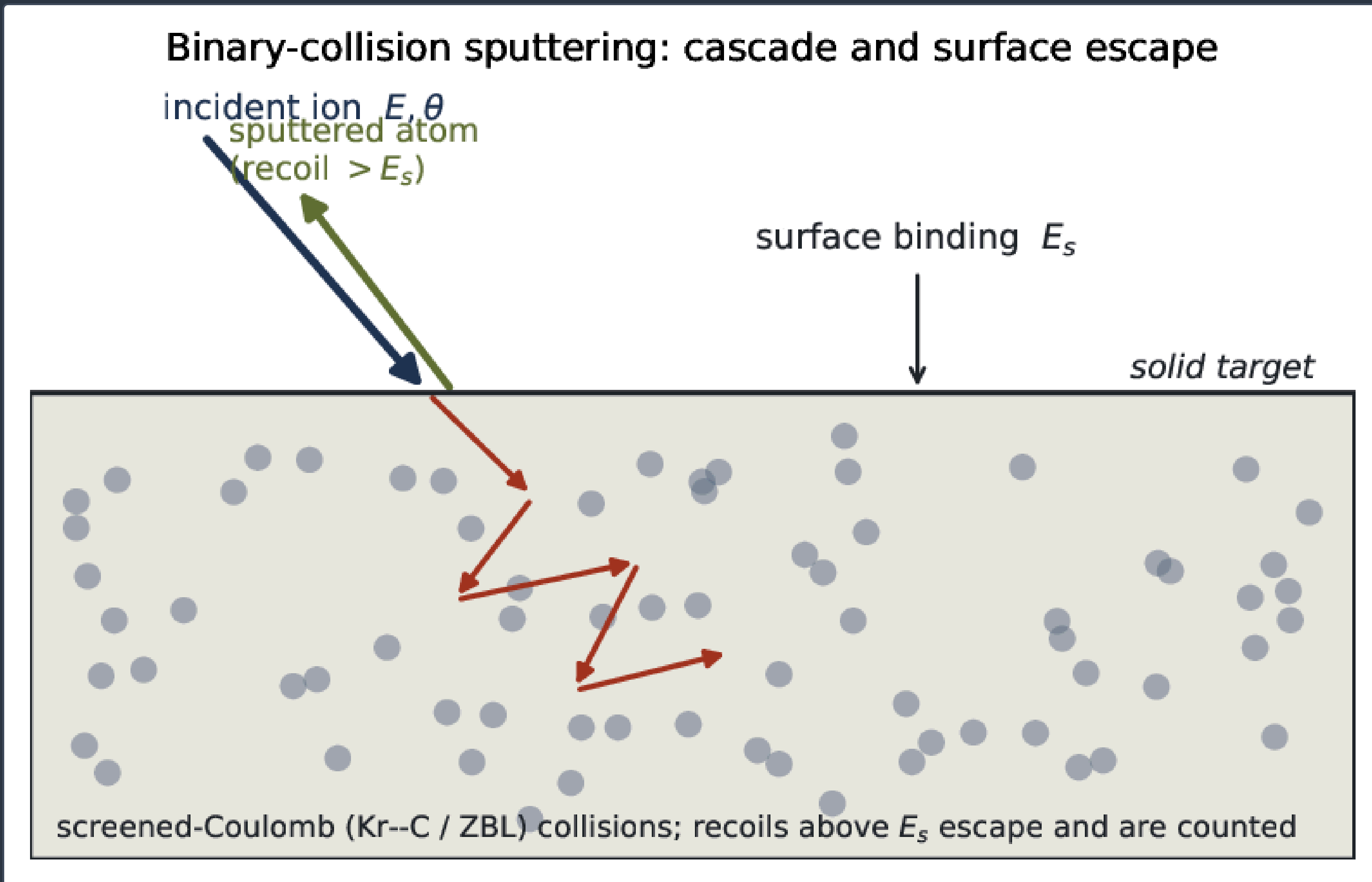

(Schematic.) Binary-collision sputtering. An incident ion of energy E and angle θ initiates a cascade of screened-Coulomb collisions; a recoil that reaches the surface with normal kinetic energy above the surface binding energy E_s escapes and is counted as sputtered (equations 1–7).

§ 6

Discussion

The physical-sputtering source term for the breeder's plasma-facing surfaces is now quantified, internally validated against its own threshold physics, and anchored to the published literature. Three comparisons place the numbers.

First, against tabulated tungsten data: the deuterium-on-tungsten yield of order 10^{-2} at ~ 1 keV and the vanishing yield below ~ 200 eV reproduce the Yamamura–Tawara and Eckstein compilations and the ITER tungsten-divertor physics basis, within which detachment is likewise the mechanism that keeps tungsten sputtering tolerable [14,16,3,18]. Our added value is not a new tungsten number but a self-consistent one: the same collision model that yields 1.35×10^{-2} at the peak yields exact zeros at 100 eV, and those zeros fall precisely where equation 11 says the threshold is, so the result is anchored at both ends of the energy range without free parameters.

Second, against the compact-ST first-wall lifetime picture: erosion is one of the four wall-lifetime channels alongside displacement damage, gas-driven swelling and fatigue, and the present source term feeds the combined first-wall and plasma-facing-component lifetime assessment and the first-wall thermomechanics analysis [33,34]. That erosion is sub-monolayer per pulse at the design point means it is not the binding wall-lifetime channel — neutron displacement damage and the consumable-centrepost fluence budget are — which is the correct and useful conclusion for a compact breeder.

Third, against the low-activation material choice: the alloy's order-of-magnitude-higher near-threshold yield is the quantified cost of the near-neutral activation composition [22,23], and the light-element-carried, self-limiting character of that erosion — through the altered layer 16 — is exactly the design-relevant detail a materials down-select needs. It says that the alloy's surface will run heavy-enriched, that the migrated impurity will be predominantly Ti and V rather than high-Z tungsten, and that the erosion penalty is bounded and falls with operating energy, all of which are favourable for a detached, cold-target divertor.

What this paper deliberately does not yet claim is the net erosion rate after redeposition and chemistry. It reports the erosion source term, honestly labelled, and hands a clean, converged reference set to the surface-evolution model that follows.

§ 7

Limitations

The yields are physical sputtering only, computed in the binary-collision approximation. Two effects are not included and both act to reduce net erosion below the source-term values reported here: chemical sputtering (negligible for these refractory metals under hydrogenic bombardment but not identically zero), and redeposition-resolved surface evolution, which returns the large prompt-redeposition fraction R of 14 and integrates the altered-layer dynamics 16 in time. Both are the one named next step, set up as the erosion/redeposition tracker (KFE-CF-BR-033) that this reference set validates. The BCA itself assumes an amorphous target and independent binary collisions, so it does not resolve crystalline channelling or many-body, high-fluence-morphology effects; for the low yields and refractory targets of interest these are second-order. The representative first-wall flux used in the recession budget is a modelling choice stated explicitly, not a measured design-point value; the yield map itself is flux-independent.

§ 8

Conclusion

Binary-collision modelling of 36 ion–surface cases fixes the physical-sputtering source term of the Hyperion breeder's plasma-facing surfaces and states it as a reproducible transport problem. Deuterium on tungsten peaks at 1.35×10^{-2} atoms\,ion^{-1}, on the literature value, and is identically zero at 100 eV because that energy lies below the analytic threshold $E_{\mathrm{th}} \simeq 213$ eV predicted by the same theory — a parameter-free internal validation. The tungsten surface peaks across all species at 8.92×10^{-2} atoms\,ion^{-1} at the helium-1000 eV corner, following the mass and energy dependence of the nuclear-stopping cross-section. The candidate low-activation divertor alloy $Ta_{32}Re_{26}W_{18}Ti_{14}V_{10}$ peaks higher, at 1.44×10^{-1} atoms\,ion^{-1}, its erosion carried by the light titanium and vanadium constituents while the heavy tungsten, tantalum and rhenium stay below threshold up to 300 eV; in steady state this drives a self-limiting, heavy-enriched altered surface layer. Converting yields to a recession budget, and closing the boundary through the sheath, shows that at the sub-threshold impact energies of detached-divertor operation the effective yield collapses and net erosion is sub-monolayer per pulse, placing the tungsten first wall firmly in the slow-erosion regime. The reference yield map anchors the surface-lifetime budget and validates the real-time erosion/redeposition tracker built on it.

Acknowledgments tocsectionAcknowledgments Part of the Kronos Fusion Energy 2026 design series. The authors thank the Kronos physics de-risking programme for the frozen result set underlying every quantitative claim, and the NVIDIA GPU HPC campaign team for the compute fleet on which the case matrix was run.

Reproducibility. The sputter-yield matrix is a frozen anchor (serial BR-L2-A27) in the Kronos Physics De-Risking Register [27] (doi:10.5281/zenodo.22133057), stamped independently re-tested and reproduced, and is regenerable byte-for-byte from the archived RustBCA inputs (fixed seed 20260726) and the figure-generation script deposited with this paper. This paper is archived at its DOI doi:10.5281/zenodo.22645885; official version: https://www.kronosfusionenergy.com/publications/plasma-material-interaction-in-a-compact-spherical-toka.html and at its official page https://www.kronosfusionenergy.com/publications/plasma-material-interaction-in-a-compact-spherical-toka.html; the register is archived at doi:10.5281/zenodo.22133057.

Data availability tocsectionData availability The 36-case RustBCA summary outputs, the harvested yield table, and the matplotlib script that generates every data figure from them are archived with the deposit at doi:10.5281/zenodo.22645885, which references the Kronos 2026 series and its de-risking register doi:10.5281/zenodo.22133057. All quantitative values trace to the register by the serial identifier BR-L2-A27 cited inline. Any economic analysis is reported separately and is not part of the public deposit. The official version of record is hosted at https://www.kronosfusionenergy.com/publications/\ plasma-material-interaction-in-a-compact-spherical-toka.html

Competing interests tocsectionCompeting interests Provisional patent applications relating to aspects of this work have been filed.

tocsectionReferences

APPARATUS

Portfolio, People & Record

The intellectual-property estate, the people who built it, the limitations that gate it, and the sources it rests on.

1	4	40	27
GRANTED PATENT	2026 PROVISIONALS	TEAM MEMBERS	2022 PROVISIONALS

INTELLECTUAL PROPERTY

The patent portfolio

The estate spans a granted high-field magnet patent, pending utility and 2026 provisional filings that map to the two products, a digital-twin control provisional, a registered trademark application, and the original 2022 provisional family. Every patentable disclosure in the five-paper arXiv drop was protected **before** publication: the breeder and burner provisionals were filed 1–2 August, and a publication-gap omnibus filing the evening before the drop swept up the DEC, plasma-control, and REBCO-winding matter of the three otherwise-unprotected papers. Patent numbers and application serials are matters of public record; claim scope is summarised, not reproduced.

GRANTED & PENDING UTILITY

US 12,009,112	High-field tilted graded-REBCO magnet architecture (KRONO-002A) · *app. 17/878,550*	GRANTED
US 17/878,507	Core device / method (KRONO-001A) · *utility*	PENDING

2026 PROVISIONAL FILINGS — MAPPED TO THE PRODUCTS

64/124,209	Hyperion — spherical-tokamak tritium / helium-3 foundry · *breeder · filed Aug 2026*	FILED
64/124,220	Aegis / MetroVolt — synchrotron-cutoff, fuel-selection & plug-winding · *generator · filed Aug 2026*	FILED
64/115,167	KRONOS-CTRL digital-twin plant control · *provisional · filed Jul 2026*	FILED
64/005,440	Integrated spherical-tokamak fusion architecture · *early integrated-architecture filing · filed Mar 2026*	FILED
64/105,530	Negative-triangularity spherical-tokamak architecture · *foundational ST filing · filed Jul 2026*	FILED
64/128,097	Publication-gap omnibus — quasineutral two-species expander DEC · provenance-gated / latency-split plasma control · as-built high-field winding & conductor architecture · *filed 7 Aug 2026, the evening before the arXiv drop*	FILED

TRADEMARK & ORIGIN

FTK-98801894	Kronos Fusion Energy — trademark application	FILED
KR-2022-*	Original provisional family (KR-2022-00001 … 00027) · *27 filings, 2022*	PRIORITY

The narrow, defensible magnet novelty — the specific conductor and the digital-twin winding optimisation, not high-field REBCO as a category — is the commercial core that can earn ahead of any Q > 1 milestone, with markets in fusion magnet supply, MRI/NMR, accelerators, and proton therapy. The claim is scoped honestly: the high field is a *system field* result, not a stand-alone-coil record; the small-bore plug coil is structurally infeasible as a bare winding but resolved by a stress-managed structural shield (feasible-pending-FEA); and the winding-tape experiment returned a *null result*. The value is the method, not a field record.

THE TEAM

Founding partners, board, advisors & auditors

Kronos is built by a bench of advanced-fuel-fusion, high-field-magnet, direct-conversion, and materials specialists, with a board and operations team drawn from defense, national laboratories, and industry. Dates are shown as ranges; where a tenure has ended or is term-ending, the range says so.

FOUNDING PARTNERS — SCIENCE

Dr. Gerald Kulcinski
Co-Founder · Helium-3 & Advanced-Fuel Fusion
UW–Madison · 2023–Present

Dr. Carl Weggel
Chief Scientist / S.M.A.R.T. Design
MIT Alcator Program · 2022–Present

Dr. Robert J. Weggel
Magnetic Field Design
MIT Magnet Lab · 2022–Present

BOARD

Priyanca Ford
Founder & CEO · Executive Board
2022–Present

Bandel Carano
Finance / Strategy
Oak Investment Partners / Stanford · 2025–2026

Patrick Schweiger
Fusion Device Engineering
Oklo / CFS / TerraPower · 2025–Present

SCIENTIFIC ADVISORS

Dr. Steven O. Dean
Fusion Policy & History
DOE / Fusion Power Associates · 2025–Present

Dr. Patrick H. Diamond
Plasma Turbulence & Transport
UC San Diego · 2025–Present

Dr. Jack J. Dongarra
HPC & Numerical Algorithms
Turing Award · 2025–Present

Dr. Nasr M. Ghoniem
Chief Material Scientist
UCLA · 2025–Present

Dr. Siegfried Glenzer
Plasma Physics & Laser Fusion
Stanford / SLAC · 2022–Present

Dr. David A. Hammer
Pulsed-Power Fusion
Cornell · 2025–Present

Dr. Donald A. Spong
Plasma Theory & Confinement
ORNL · 2025–Present

Dr. Curtis Smith
Risk Assessment & Nuclear PRA
MIT / Idaho National Lab · 2025–Present

RADM (Ret.) David Goggins
Naval Engineering & Power-Plant Design
U.S. Navy · 2023–2026

Dr. Konstantin Batygin
Mathematician
Caltech · 2022–2025

Dr. Ruben Fair
Magnet Design / ITER Liaison
PPPL / Jefferson Lab · 2022–2025

Dr. Paul S. Weiss
Materials & Nanotechnology
UCLA · 2022–2025

SCIENTIFIC AUDITORS

Dr. Wilfred A. Cooper
Plasma Equilibrium Theory
EPFL / Swiss Plasma Center · 2025–Present

Dr. Ahmed Hassanein
Plasma–Material Interactions
Purdue / Argonne · 2025–Present

Dr. Patrick E. Hopkins
Extreme Thermal Materials
U. of Virginia · 2025–Present

Dr. Peter Hosemann
Materials Joining & Structural Integrity
UC Berkeley · 2025–Present

Dr. Travis W. Knight
Advanced Nuclear Fuels & Systems
U. of South Carolina · 2025–Present

Dr. Philippe Lebrun
Cryogenics & Magnet Cooling
CERN · 2025–Present

Dr. Nitendra Singh
Nuclear Safety & Fuel Cycle
ITER · 2025–Present

Dr. Guido Van Oost
Magnetic Confinement & Fusion Systems
Ghent University · 2025–Present

Dr. Gary S. Was
Radiation Materials & Structural Integrity
U. of Michigan · 2025–Present

Dr. Ray Sedwick
Direct Energy Conversion
U. of Maryland · 2025

OPERATIONS

Michael Laughlin
Chief Operating Officer
2022–Present

Martin Owens
Chief Strategy Officer
LANL / GE Hitachi · 2022–Present

MG (Ret.) Paul Pardew
Chief Contracting Officer
Army Contracting Command · 2022–Present

David Beck
Fusion Commercialization
U.S. Space Force · 2024–Present

Sushma Bhatia
Environmental & Legislative
Google · 2022–Present

Michael De Frenza
Technology Licensing
2023–Present

MG (Ret.) Robin L. Fontes
Cybersecurity & Defense
Army Cyber Command · 2022–Present

Vijay Gehani
Supply Chain & Components
INOX India · 2024–Present

Jon Michel Greenwood
IT & AI Infrastructure
Live Nation · 2023–Present

Brian C. O'Neill
National Security
CIA / ODNI · 2022–Present

Gen. (Ret.) Gustave F. Perna
DoD Liaison
Operation Warp Speed · 2022–2023

Andrea Romero
Marketing Lead
2022–Present

Legal counsel is retained; those roles are held on the internal roster and are not listed here.

SOURCES

References

1 G Federici *et al*, Plasma-material interactions in current tokamaks and their implications for next step fusion reactors, *Nucl. Fusion* **41** 1967 (2001). doi:10.1088/0029-5515/41/12/218

2 J Roth *et al*, Recent analysis of key plasma wall interactions issues for ITER, *J. Nucl. Mater.* **390–391** 1 (2009).

3 R A Pitts *et al*, Physics basis for the first ITER tungsten divertor, *Nucl. Mater. Energy* **20** 100696 (2019).

4 D Naujoks, K Asmussen, M Bessenrodt-Weberpals *et al*, Tungsten as target material in fusion devices, *Nucl. Fusion* **36** 671 (1996).

5 A Kirschner, V Philipps, J Winter and U K\"ogler, Simulation of the plasma-wall interaction in a tokamak with the Monte Carlo code ERO-TEXTOR, *Nucl. Fusion* **40** 989 (2000).

6 J N Brooks, Modeling of sputtering erosion/redeposition — status and implications for fusion design, *Fusion Eng. Des.* **60** 515 (2002).

7 P I Ford, Hyperion as a strategic-materials platform: gain, tritium breeding, He-3 co-production, and 14 MeV neutron output from a compact spherical tokamak, Kronos Fusion Energy 2026 series. doi:10.5281/zenodo.22645691; kronosfusionenergy.com/publications/breeder.html

8 J E Menard *et al*, Fusion nuclear science facilities and pilot plants based on the spherical tokamak, *Nucl. Fusion* **56** 106023 (2016). doi:10.1088/0029-5515/56/10/106023

9 B N Sorbom *et al*, ARC: a compact, high-field, fusion nuclear science facility and demonstration power plant with demountable magnets, *Fusion Eng. Des.* **100** 378 (2015). doi:10.1016/j.fusengdes.2015.07.008

10 A Loarte *et al*, Chapter 4: Power and particle control, *Nucl. Fusion* **47** S203 (2007).

11 P I Ford and G L Kulcinski, A divertor-exhaust concept down-select for a compact spherical-tokamak breeder: Super-X, snowflake, X-point-target and liquid-metal geometries ranked by peak heat flux and detachment window, Kronos Fusion Energy 2026 series. doi:10.5281/zenodo.22645933; kronosfusionenergy.com/publications/a-divertor-exhaust-concept-down-select-for-a-compact-sp.html

12 P Sigmund, Theory of sputtering. I. Sputtering yield of amorphous and polycrystalline targets, *Phys. Rev.* **184** 383 (1969).

13 J Bohdansky, A universal relation for the sputtering yield of monatomic solids at normal ion incidence, *Nucl. Instrum. Methods Phys. Res. B* **2** 587 (1984).

14 Y Yamamura and H Tawara, Energy dependence of ion-induced sputtering yields from monatomic solids at normal incidence, *At. Data Nucl. Data Tables* **62** 149 (1996). doi:10.1006/adnd.1996.0005

15 J P Biersack and L G Haggmark, A Monte Carlo computer program for the transport of energetic ions in amorphous targets, *Nucl. Instrum. Methods* **174** 257 (1980).

16 W Eckstein, *Computer Simulation of Ion-Solid Interactions*, Springer Series in Materials Science **10** (Springer, Berlin, 1991).

17 W M\"oller and W Eckstein, Tridyn — a TRIM simulation code including dynamic composition changes, *Nucl. Instrum. Methods Phys. Res. B* **2** 814 (1984).

18 G De Temmerman, T Hirai and R A Pitts, The influence of plasma-surface interaction on the performance of tungsten at the ITER divertor vertical targets, *Plasma Phys. Control. Fusion* **60** 044018 (2018).

19 J Roth and K Schmid, Hydrogen in tungsten as plasma-facing material, *Phys. Scr.* **T145** 014031 (2011).

20 Y Ueda *et al*, Baseline high heat flux and plasma facing materials for fusion, *Nucl. Fusion* **57** 092006 (2017).

21 R Ding *et al*, Advances in understanding of high-Z material erosion and re-deposition in low-Z wall environment in DIII-D, *Nucl. Fusion* **57** 056016 (2017).

22 P I Ford and G L Kulcinski, First-principles near-neutral low-activation refractory alloys for fusion plasma-facing components, Kronos Fusion Energy 2026 series. doi:10.5281/zenodo.22645744; kronosfusionenergy.com/publications/low-activation-alloys.html

23 P I Ford and G L Kulcinski, A tantalum- and rhenium-free low-activation alloy family for first wall, divertor and direct-energy-converter electrodes. Kronos Fusion Energy 2026 series. doi:10.5281/zenodo.22645891; kronosfusionenergy.com/publications/a

COLOPHON

How this document was made

The Kronos Fleet — Combined Editorial, 2026 is set in **Fraunces** (display), **Gelasio** (text), and **IBM Plex Mono** (data & equations), carried forward from the Kronos editorial design system.

The figures are rendered at 300 dpi from the deposited generator scripts; the document is composed as a single self-contained file with embedded fonts and imagery, paginated to US Letter, and rendered to PDF through a headless Chromium engine in matched light and dark editions.

Every headline quantity carries an evidence class; withdrawn and restated values are marked as such. Nothing herein is frozen beyond the founder-approved Tier-A set.

Explore it live — turn the interactive 3-D model, run the deposited solvers in the physics validator, and watch the companion film series.

LEGAL NOTICE

Notice, status, and distribution

Conceptual design & simulation study. This document reports a conceptual design and simulation study. It is not a construction commitment, a safety-analysis report, a regulatory filing, or an offer of securities. Forward-looking statements — schedules, costs, market sizes, and performance — are estimates subject to the limitations set out in the Simulations part and may change.

Numbers and their classes. Quantities are reported with evidence classes and case labels; modelled, assumed, and requirement-class values are identified as such and are not to be quoted without their labels.

Public edition. This edition carries the physics and design only; all financial, funding, and defense-commercial content has been removed for public distribution. The scientific text corresponds to the arXiv and journal submissions.

THE 2026 KRONOS SERIES

One programme, many papers

This editorial is one paper in the Kronos 2026 series — a real fusion company's complete, reproducible physics record for a spherical-tokamak breeder and its low-neutron D–^{3}He tandem-mirror burners. Every headline number is a frozen anchor in the Physics De-Risking Register.

Explore the whole programme: the De-Risking Register, the interactive 3-D model, and the physics validator.

KRONOS FUSION ENERGY

Plasma-Material Interaction in a Compact Spherical-Tokamak Breeder: Sputtering, Net Erosion, and Redeposition Setting the Plasma-Facing-Surface Lifetime

A real fusion company building real machines. Explore the science, live.

Zenodo · doi:10.5281/zenodo.22645885

Read on kronosfusionenergy.com

The Physics De-Risking Register